ARTICLE Open Access

Highly DUV to NIR-II responsive broadband quantum dots heterojunction photodetectors by integrating quantum cutting luminescent concentrators

Nan Ding¹, Wen Xu^{1⊠}, Hailong Liu¹, Yuhan Jing¹, Zewen Wang¹, Yanan Ji¹, Jinlei Wu¹, Long Shao¹, Ge Zhu^{1⊠} and Bin Dong^{1⊠}

Abstract

Low-cost, high-performance, and uncooled broadband photodetectors (PDs) have potential applications in optical communication etc., but it still remains a huge challenge to realize deep UV (DUV) to the second near-infrared (NIR-II) detection for a single broadband PD. Herein, a single PD affording broadband spectral response from 200 to 1700 nm is achieved with a vertical configuration based on quantum dots (QDs) heterojunction and quantum cutting luminescent concentrators (QC–LC). A broadband quantum dots heterojunction as absorption layer was designed by integrating CsPbl₃:Ho³⁺ perovskite quantum dots (PQDs) and PbS QDs to realize the spectral response from 400 to 1700 nm. The QC–LC by employing CsPbCl₃:Cr³⁺, Ce³⁺, Yb³⁺, Er³⁺ PQDs as luminescent conversion layer to collect and concentrate photon energy for boosting the DUV–UV (200–400 nm) photons response of PDs by waveguide effect. Such broadband PD displays good stability, and outstanding sensitivity with the detectivity of 3.19×10^{12} Jones at 260 nm, 1.05×10^{13} Jones at 460 nm and 2.23×10^{12} Jones at 1550 nm, respectively. The findings provide a new strategy to construct broadband detector, offering more opportunities in future optoelectronic devices.

Introduction

Photodetectors (PDs) with the ability to capture optical signals and convert them into electrical signals, are significance in optoelectronic applications^{1–4}. Particularly, uncooled broadband PDs capable of covering the near infrared (NIR) region with low-cost and high-performance are vital components for optical communication, national security, military monitoring, and bioimaging^{5–7}. Currently, the commercial broadband PDs were fabricated by mature materials with narrow bandgap, such as silicon (Si), indium gallium arsenide (InGaAs), and mercury cadmium telluride (HgCdTe) etc. With the rapid development of detection technology, they achieved

excellent response within visible to short-wave-NIR (eg., Si PDs)⁸ or the second near-infrared (NIR-II) region (eg., InGaAs PDs)⁹. However, to our knowledge, few of them are targeted to realize high performance in the whole region spanning from deep ultraviolet (DUV) to NIR-II. Previously, to construct fully spectral responsive PDs, two or more PDs should be integrated into one system, inevitably bringing about large size, high price, and especially for incomparable responsiveness among different PDs. Meanwhile, these PDs usually encounter with complex fabrication process and low temperature working conditions etc. All of these cause huge difficulties in practical applications.

All inorganic lead halide (CsPbX₃, X = Cl, Br or I) perovskite quantum dots (PQDs) have attracted numerous attention in solar cells, light-emitting diodes (LEDs), lasers and PDs, owing to their excellent light sensitivity, tunable bandgap, large absorption coefficient, and high

Correspondence: Wen Xu (xuwen@dlnu.edu.cn) or

Ge Zhu (zhuge@dlnu.edu.cn) or Bin Dong (dong@dlnu.edu.cn)

¹Key Laboratory of New Energy and Rare Earth Resource Utilization of State Ethnic Affairs Commission, School of Physics and Materials Engineering, Dalian Minzu University, 18 Liaohe West Road, Dalian 116600, China

© The Author(s) 2024

Open Access This article is licensed under a Creative Commons Attribution 4.0 International License, which permits use, sharing, adaptation, distribution and reproduction in any medium or format, as long as you give appropriate credit to the original author(s) and the source, provide a link to the Creative Commons licence, and indicate if changes were made. The images or other third party material in this article are included in the article's Creative Commons licence, unless indicated otherwise in a credit line to the material. If material is not included in the article's Creative Commons licence and your intended use is not permitted by statutory regulation or exceeds the permitted use, you will need to obtain permission directly from the copyright holder. To view a copy of this licence, visit http://creativecommons.org/licenses/by/4.0/.

collection efficiency of carriers^{10–16}. Especially, iodine based PQDs process narrow bandgap (~1.73 eV) with a wide spectral response, exhibiting a great potential for photoactive layer to constructing broadband PDs^{17–19}. Nevertheless, the current PDs based on CsPbI₃ PQDs still suffer from low sensitivity, slow response time, and poor stability, due to the high trap density and susceptibility to UV light and oxygen^{20–22}. In addition, its responsive wavelength was concentrated in UV–Visible region (350 nm–750 nm), uncapable of covering the DUV–UV (200 nm–350 nm) and NIR (>750 nm) because of the insensitivity for DUV–UV light and limitation of bandgap^{23,24}. Therefore, how to overcome the above issues as the main challenges for obtaining broadband and high performance PDs.

Doping with lanthanide ions (eg.,Ce³⁺, Eu³⁺, Eu²⁺, Sm³⁺, Nd³⁺, Er³⁺) has emerged to boost the optical and electrical performance of PQDs, such as improving the photoluminescence quantum yields (PLOYs), enhancing UV- and long term- stability, and decreasing the trap density^{25–29}. It is mainly assigned to their unique spectroscopic properties and atomic radii suitable for the tolerance factor of PODs^{13,27,30–32}. Meanwhile, a hybrid structure combining perovskites with the organic or inorganic narrower bandgap semiconductor materials (e.g.,BTP-4Cl:PBDB-TF, PbSe, HgTe, PbS) is one of a promising strategy to achieve high performance broadband PDs with NIR spectral response^{33–35}. Among them, lead sulfide (PbS) quantum dots (QDs) with easily adjustable absorption range to the NIR-II region via the size dependent quantum confinement^{36,37}. Besides, it has large absorption coefficient (~10⁶ M⁻¹ cm⁻¹) and better chemical stability³⁸

Aiming at the low DUV-UV response of PDs, the downshifting luminescence materials provide an effective route to convert DUV-UV light into visible or NIR photons, and subsequently being recaptured by the integrated PDs^{8,23}. Various luminescent conversion materials including the quantum cutting materials with the PLQYs of ~200% have been implemented to significantly improve the UV response of solar cells or PDs (eg., Si and perovskites)^{39,40}. But the huge photon energy loss by directly integrating with photoelectric devices always happens, stemming from the random emission direction of luminescent conversion materials. Luminescent concentrator (LC) devices with directional emission consisting of transparent polymer sheets doped with luminescent species can collect and concentrate photon energy to minimize the photons loss through waveguide effect.

In this work, high PLQYs (93.5%) and stability, and less defects of CsPbI₃:Ho³⁺ PQDs were synthesized, served as the UV–Visible photoresponsivity layer for broadband PDs. To broaden the NIR-II response of broadband PDs, the PbS QDs with Visible-NIR absorption region were directly assembled on the surface of CsPbI₃:Ho³⁺ PQDs to

form a heterojunction composite. Meanwhile, the Cr^{3+} , Ce^{3+} , Yb^{3+} , Er^{3+} doped $CsPbCl_3$ PQDs with the high PLQYs (~179%) were incorporated into the polymethyl methacrylate to prepare a quantum cutting LC (QC–LC), which can convert DUV–UV light into NIR photons and subsequently being recaptured by the integrated PDs. This broadband PDs consists of QC–LC and $CsPbI_3$:Ho³⁺ - PbS QDs heterojunction to realize the full spectrum response spanning from 200 nm–1700 nm, showing the detectivity of 3.19×10^{12} Jones at 260 nm, 1.05×10^{13} Jones at 460 nm, and 2.23×10^{12} Jones at 1550 nm. Furthermore, this broadband PDs demonstrate outstanding air- and UV-stability and high-contrast imaging applications.

Results

In general, the commercial broadband PDs (UV-NIR) usually by integrating two or more PDs (eg., GaN, Si, and InGaAs) for detecting DUV to UV, Visible to short-wave— NIR, and NIR light (Fig. 1a), respectively, which can bring complex fabrication process and higher costs. Herein, we successfully fabricated a broadband responsive PD from DUV to NIR-II (200 nm-1700 nm) with the device structures of CsPbCl₃:Cr³⁺, Ce³⁺, Yb³⁺, Er³⁺ PODs doped polymethyl methacrylate QC-LC / FTO / SnO₂ / CsPbI₃:Ho³⁺ - PbS QDs heterojunction / MoO₃ / Au, as shown in Fig. 1b. The corresponding cross-sectional scanning electron microscope (SEM) image of the broadband PD is displayed in Fig. S1. In such devices, the CsPbI₃:Ho³⁺ PQDs with outstanding optoelectronic performance is responsible for UV-Visible light (350 nm-700 nm). The PbS QDs were prepared through hot injection method exhibits broadband absorption from 500 nm to 1700 nm (Fig. 1c). Then, they were assembled on the surface of CsPbI₃:Ho³⁺ PODs via mechanical stirring, serving as the NIR-II absorption material. Finally, QC-LC with the strong absorption from 200 nm to 400 nm and efficiently converts them into typical NIR emission of Yb3+ and Er3+ through quantum cutting process (Fig. 1d). Consequently, these NIR photons can be further reabsorbed by the CsPbI₃:Ho³⁺— PbS QDs heterojunction, thereby expanding the response in DUV to UV region (Fig. 1e).

To obtain the high performance and broadband response in a single PD, a series of optical and electrical experiments were conducted. Firstly, to improve the performance of PQDs, lanthanide ions ($\mathrm{Ho^{3+}}$) was selected as dopant to incorporate into CsPbI $_3$ PQDs prepared by modified hot injection method^{41–43}. As revealed in the transmission electron microscope (TEM) and high-resolution TEM (HR-TEM) images (Fig. 2a and S2–S4), the undoped CsPbI $_3$ and CsPbI $_3$:Ho $^{3+}$ PQDs with the similar cubic shape were obtained. The average size of CsPbI $_3$ PQDs is ~11.6 nm, which gradually decreases to ~11.4 nm, ~11.1 nm, ~10.8 nm and ~10.5 nm with increasing $\mathrm{Ho^{3+}}$ concentrations from 1.4% to 8.3%,

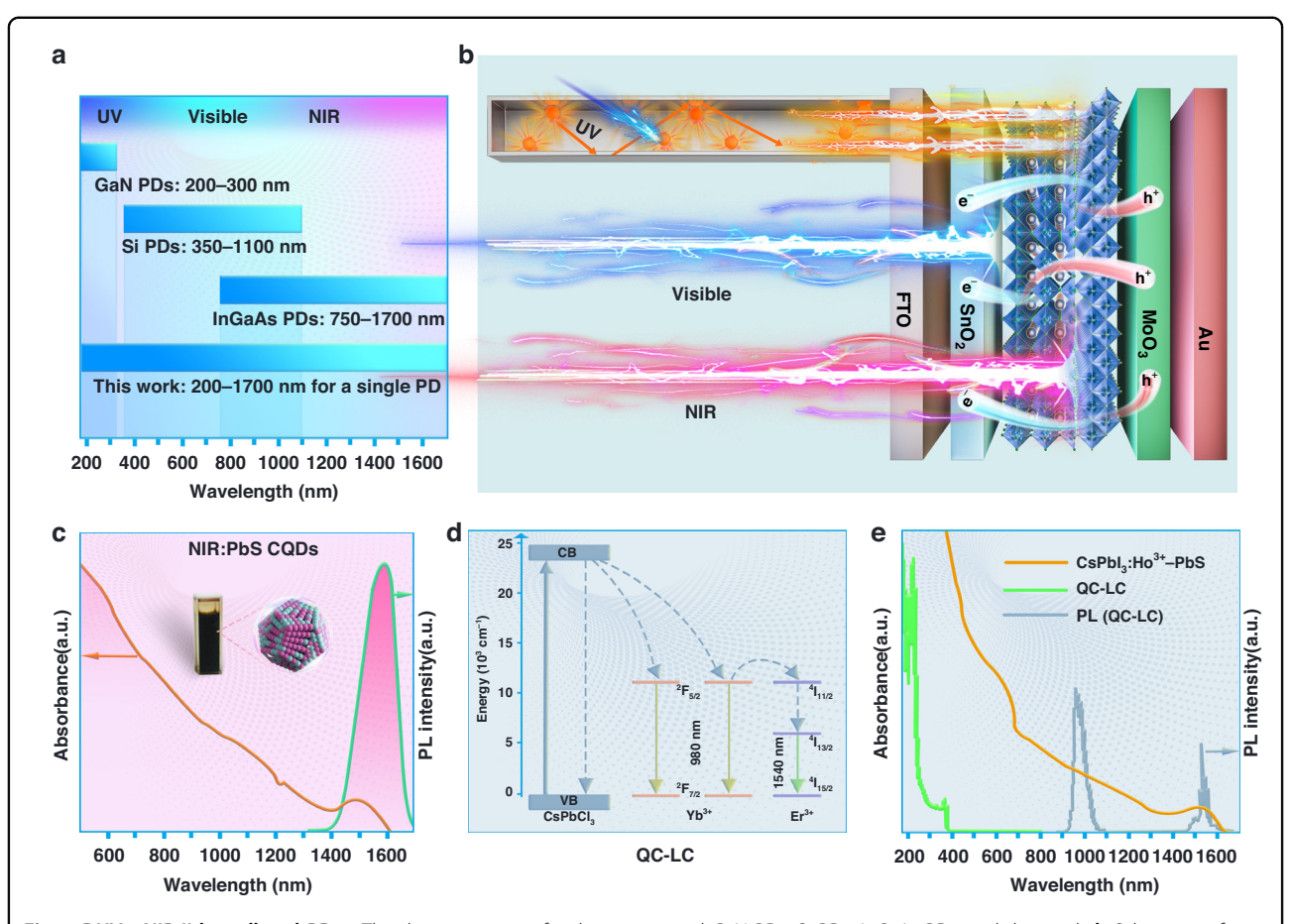


Fig. 1 DUV—NIR-II broadband PD. a The detection range for the commercial GaN PDs, Si PDs, InGaAs PDs, and this work. **b** Schematic of a broadband PD configuration. **c** Absorption and emission spectra of PbS QDs. Inset is the image of PbS QDs. **d** Energy level diagram of QC–LC. **e** Absorption spectra of QC–LC and CsPbI₃:Ho³⁺—PbS QDs, and emission spectra of QC–LC

respectively (Fig. S5). The practical Ho³⁺ doping concentration was identified by the inductively coupled plasma optical emission spectrometry (ICP-OES) and the X-ray photoelectron spectroscopy (XPS) (Table S1). The lattice distances of the (100) plane of undoped CsPbI₃ and $CsPbI_3:Ho^{3+}$ PQDs are determined to be ~6.3 Å and ~6.2 Å. The lattice shrinkage is ascribed to the replacement of the larger radius of Pb2+ (~119 pm) by smaller size of Ho^{3+} (~90.1 pm) $^{44-46}$. The energy dispersive X-ray (EDX) mapping images demonstrate that all of the elements (cesium, lead, iodine, and holmium) exist in CsPbI₃:Ho³⁺ PQDs (Fig. S6). The X-ray diffraction (XRD) patterns in Fig. S7 shows that undoped CsPbI₃ and CsPbI₃:Ho³⁺ PQDs have the same cubic structure without impurity peak, and the (100) peaks of PQDs gradually shift to higher diffraction angle after Ho³⁺ doping. Meanwhile, the XPS survey spectra evidence that the appearance of Ho3+ 4d peaks in CsPbI3:Ho3+ PQDs, and the peaks of Cs^+ 3d, Pb^{2+} 4f, and I^- 3d are presented in undoped CsPbI₃ and CsPbI₃:Ho³⁺ PQDs (Fig. 2b and S8). Compared with the undoped CsPbI₃ PQDs, the binding energy of $Pb^{2+} {}^4f_{5/2}$ and ${}^4f_{7/2}$ moves to lower energy after Ho^{3+} doping, while $Cs^+ 3d$ and $I^- 3d$ shows slight changes. Based on the above observations, we confirm that Ho^{3+} ions are successfully doped into the $CsPbI_3$ PQDs and mainly replace the Pb^{2+} sites.

Figure 2c shows the absorption and emission spectra of pristine CsPbI₃ and CsPbI₃:Ho³⁺ PQDs with various Ho³⁺ doping concentration. The absorption peak of CsPbI₃ PODs gradually blue shifts from 683 nm to 678 nm with increasing Ho³⁺ concentration. In line with the absorption peak variation, the exciton bandgap increases from 1.76 eV of pristine CsPbI3 to 1.82 eV of CsPbI₃:Ho³⁺ (6.4%) (Fig. S9). It can be mainly due to the lattice contraction by substituting Pb²⁺ with Ho³⁺ (Supplementary Note 1)47,48. Accordingly, the exciton emission peak of CsPbI₃ PQDs moves to high energy from 693 nm to 685 nm with Ho³⁺ doping (Fig. S10). Significantly, after Ho³⁺ doping, the emission intensity of CsPbI₃ PQDs rapidly enhances with the optimal Ho³⁺ concentration of 6.4%. The PLQYs of CsPbI₃:Ho³⁺ PQDs reaches remarkable 93.5% (Fig. 2d). In addition, the

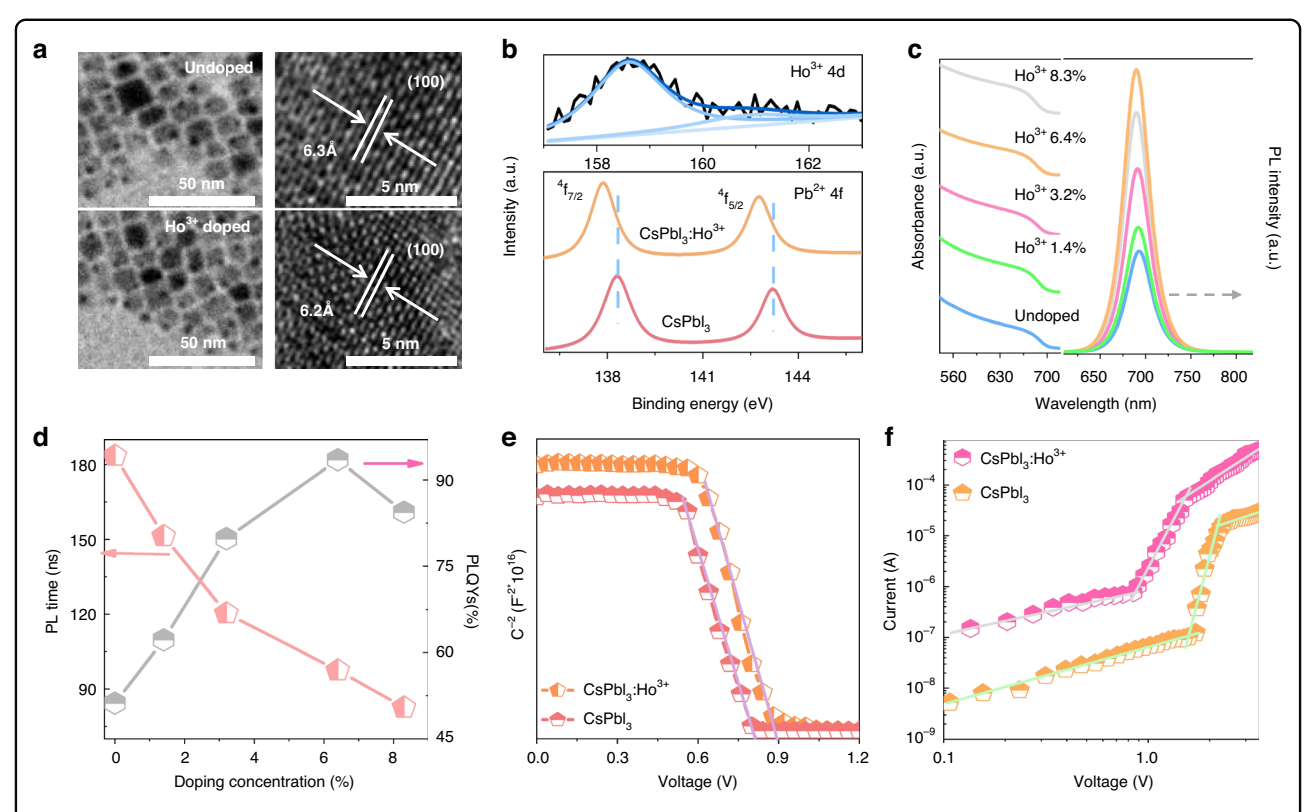


Fig. 2 Ho3+ doped CsPbl3 PQDs. a TEM and HR-TEM (right) of undoped CsPbl₃ and CsPbl₃:Ho³⁺ (6.4%) PQDs. **b** XPS spectra of Ho³⁺ (4*d*) and Pb²⁺ (4*f*) of undoped CsPbl₃ and CsPbl₃:Ho³⁺ (6.4%) PQDs. Absorption and emission spectra (**c**), and PLQYs and PL lifetime (**d**) of undoped CsPbl₃ and CsPbl₃:Ho³⁺ PQDs with different Ho³⁺ concentrations. **e** Mott–Schottky of CsPbl₃ and CsPbl₃:Ho³⁺ (6.4%) PQDs. **f** I-V curves with electron-only devices based on CsPbl₃ and CsPbl₃:Ho³⁺ (6.4%) PQDs

exciton decay lifetimes gradually decrease from 183.5 ns of pristine CsPbI $_3$ PQDs to 82.6 ns of CsPbI $_3$:Ho $^{3+}$ (8.3%) PQDs (Fig. S12). Then, the radiative rates (k_r) and non-radiative rates (k_{nr}) of CsPbI $_3$ and CsPbI $_3$:Ho $^{3+}$ PQDs were calculated according to their PLQYs and PL decay lifetimes. As displayed in Table S2, the k_r of PQDs increases about 3.44 folds from 2.79 × 10 6 S $^{-1}$ of undoped CsPbI $_3$ PQDs to 9.59 × 10 6 S $^{-1}$ of CsPbI $_3$:Ho $^{3+}$ (6.4%) PQDs. The k_{nr} of CsPbI $_3$ PQDs is 2.66 × 10 6 S $^{-1}$, which decreases to 0.67 × 10 6 S $^{-1}$ of CsPbI $_3$:Ho $^{3+}$ (6.4%) PQDs. Compared to the undoped CsPbI $_3$ PQDs, the k_r process becomes dominant for CsPbI $_3$:Ho $^{3+}$ PQDs, leading to the high emission efficiency of CsPbI $_3$:Ho $^{3+}$ (6.4%) PQDs. Based to the formula⁴⁴:

$$k_r = \frac{ne^2 \omega^2}{3\varepsilon_0 m_0 c^3} f_0 \left(\frac{\mu}{M} E_b\right)^{1.5} \frac{1 - e^{\frac{-\Delta E}{kT}}}{\Delta E}$$
 (1)

where μ , k, m_0 , ε_0 , ΔE , ω , and n are the equivalent mass of exciton, the Boltzmann's constant, the mass of exciton, the vacuum permittivity, the energy line width of PQDs, the optical transition frequency and the refractive index. The k_r can be mainly related to the exciton binding energy (E_b) of PQDs. The E_b is achieved from the temperature-

dependent PL intensity of PQDs by²¹:

$$I_{(T)} = \frac{I_0}{1 + A \exp\left(\frac{-E_b}{kT}\right)} \tag{2}$$

where the I_0 is the PL intensity of PQDs at 0 k, A is the proportional constant. The E_b of CsPbI $_3$:Ho $^{3+}$ (6.4%) PQDs is 32.8 meV (Fig. S13), and 20 meV for pristine CsPbI $_3$ PQDs 49 . On the basis of Eq. (1), it suggests that the increasing k_r with Ho $^{3+}$ doping is mainly originates from the increase of the E_b of PQDs.

The role of $\mathrm{Ho^{3+}}$ on the electrical performance of PQDs films were investigated using I-V curves. As shown in Fig. S14 and Supplementary Note 2, the conductivity (σ) was determined to be $1.18 \times 10^{-6} \, \mathrm{S \, cm^{-1}}$ for the pristine CsPbI₃ PQDs, which increases to $3.54 \times 10^{-6} \, \mathrm{S \, cm^{-1}}$ in CsPbI₃:Ho³⁺ PQDs. The Mott–Schottky analysis was used to obtain the built-in potential (V_{bi}) of the devices through capacitance-voltage (C-V) measurements (Fig. 2e and Supplementary Note 3). The CsPbI₃:Ho³⁺ PQDs exhibits higher V_{bi} (\sim 0.89 V) than that of the undoped CsPbI₃ PQDs (\sim 0.81 V), indicating the decreased carrier accumulation and improved carrier transports in PDs⁵⁰. Meanwhile, according

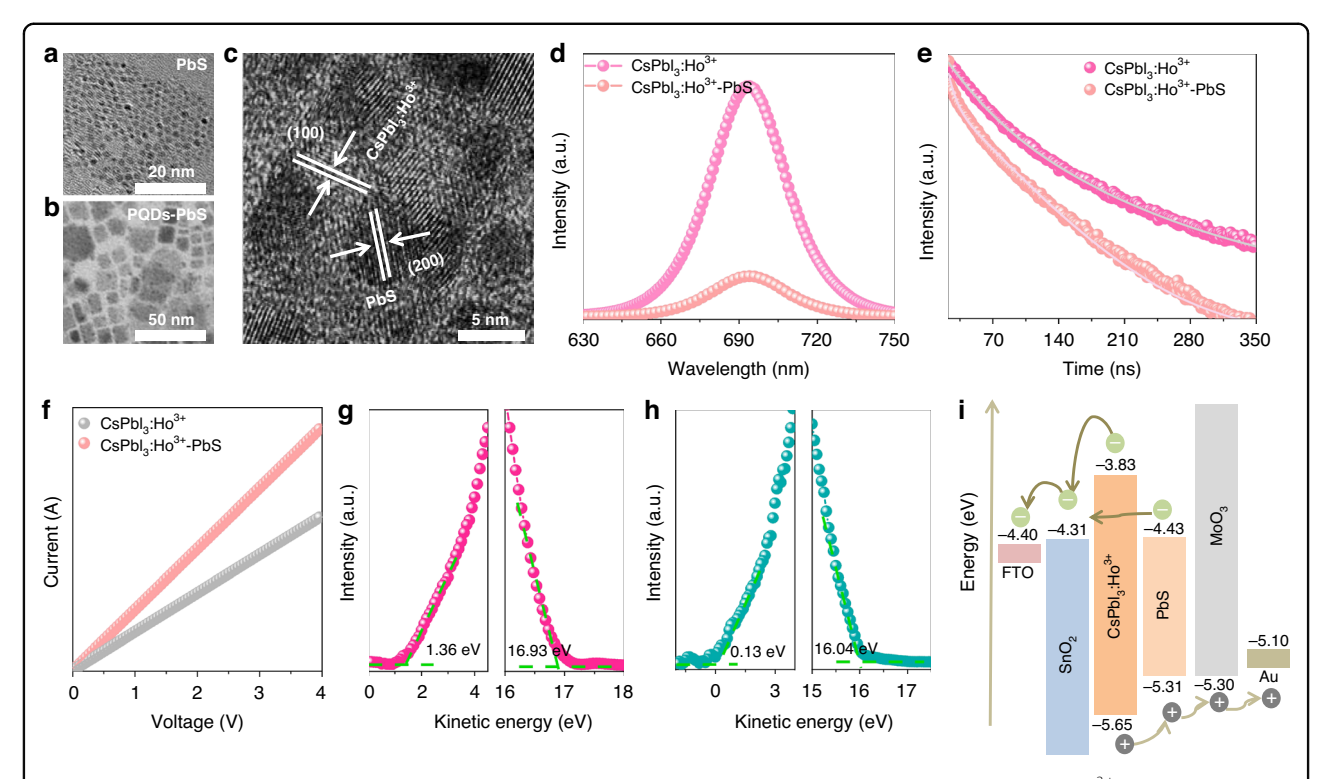


Fig. 3 Photoelectric characteristics of CsPbl3:Ho3+- PbS QDs heterojunction. TEM images of PbS QDs (**a**) and CsPbl₃:Ho³⁺—PbS QDs (**b**). **c** HR-TEM image of CsPbl₃:Ho³⁺—PbS QDs. **d** Emission spectra of CsPbl₃:Ho³⁺ PQDs and CsPbl₃:Ho³⁺ - PbS QDs. **e** PL lifetime of CsPbl₃:Ho³⁺ PQDs and CsPbl₃:Ho³⁺—PbS QDs at 692 nm. **f** *I-V* curves of CsPbl₃:Ho³⁺ PQDs and CsPbl₃:Ho³⁺—PbS QDs. UPS curves of CsPbl₃:Ho³⁺ PQDs (**g**) and PbS QDs (**h**). The Fermi level of CsPbl₃:Ho³⁺ PQDs and PbS QDs are -4.29 eV and -5.18 eV, respectively. **i** Schematic illustration of the each layer in PDs

to the space charge limited current (SCLC) method, the trap density of undoped CsPbI₃ and CsPbI₃:Ho³⁺ PQDs were deduced to be $1.05 \times 10^{17} \, \text{cm}^{-3}$ and $4.08 \times 10^{16} \, \text{cm}^{-3}$ (Fig. 2f and Supplementary Note 4). It reduces 2.57 folds of CsPbI₃ PQDs with Ho³⁺ doping, dominating the decrease of k_{nr} for CsPbI₃:Ho³⁺ PQDs. The charge carrier mobility increases from $6.35 \times 10^{-4} \, \mathrm{cm^2 \, V^{-1} \, S^{-1}}$ of pristine CsPbI₃ PQDs to $4.94 \times 10^{-3} \, \mathrm{cm^2 \, V^{-1} \, S^{-1}}$ of CsPbI₃:Ho³⁺ PQDs. Furthermore, the air- and UV- stability of CsPbI₃ PQDs significantly improves after Ho³⁺ doping (Fig. S15). It can be seen that the emission intensity of undoped CsPbI₃ PQDs degrades rapidly, almost disappears after 8 days storage and 12 h UV irradiation. In contrast, the emission intensity of CsPbI₃:Ho³⁺ PQDs maintains about 95% and 90% of the original intensity after 50 days storage and 24 h UV radiation. The tolerance factor of CsPbI₃:Ho³⁺ PQDs was estimated to be 0.813, larger than that 0.807 of pristine CsPbI₃ PQDs (Fig. S16). Therefore, reduced trap density, boosted the carrier mobility and conductivity, enhanced the stability, and increased tolerance factor of CsPbI₃ PODs with Ho³⁺ doping account for the improved performance for broadband PDs based on CsPbI₃:Ho³⁺ PODs.

We next performed the optical and electrical analysis of $CsPbI_3$: Ho^{3+} PQDs by combining with PbS QDs. As shown in Fig. 3a and S17–S18, the PbS QDs exhibits

the cubic shape with an average diameter of ~4.4 nm were obtained by typical hot injection method⁵¹. Then, the smaller sized PbS QDs would attach on the CsPbI₃:Ho³⁺ PQDs surface to formation of a heterojunction composite by electrostatic interactions (Fig. 3b and S19). We further revealed the HR-TEM of CsPbI₃:Ho³⁺—PbS QDs heterojunction, in which the lattice plane of CsPbI₃:Ho³⁺ (100) and PbS (200) can be clearly identified (Fig. 3c). The CsPbI₃:Ho³⁺—PbS QDs heterojunction exhibits a complementary absorption in the visible to NIR-II region (400 nm-1700 nm), where the enhanced absorption within 400 nm-681 nm is corresponding to exciton absorption of CsPbI₃:Ho³⁺ PQDs (Fig. S20). The PL intensity of CsPbI₃:Ho³⁺ PQDs dramatically reduces after integrating with PbS QDs (Fig. 3d), accompanied by the shortening of exciton lifetime of CsPbI₃:Ho³⁺ PQDs from 97.5 ns to 62.3 ns for CsPbI₃:Ho³⁺—PbS QDs heterojunction (Fig. 3e). Those results indicate that the CsPbI₃:Ho³⁺— PbS QDs heterojunction can effective improve the carrier extraction and transfer. Meanwhile, the NIR emission of PbS QDs slightly increases CsPbI₃:Ho³⁺—PbS QDs heterojunction under 808 nm excitation (Fig. S21), enabling the high responsivity of PDs in NIR region.

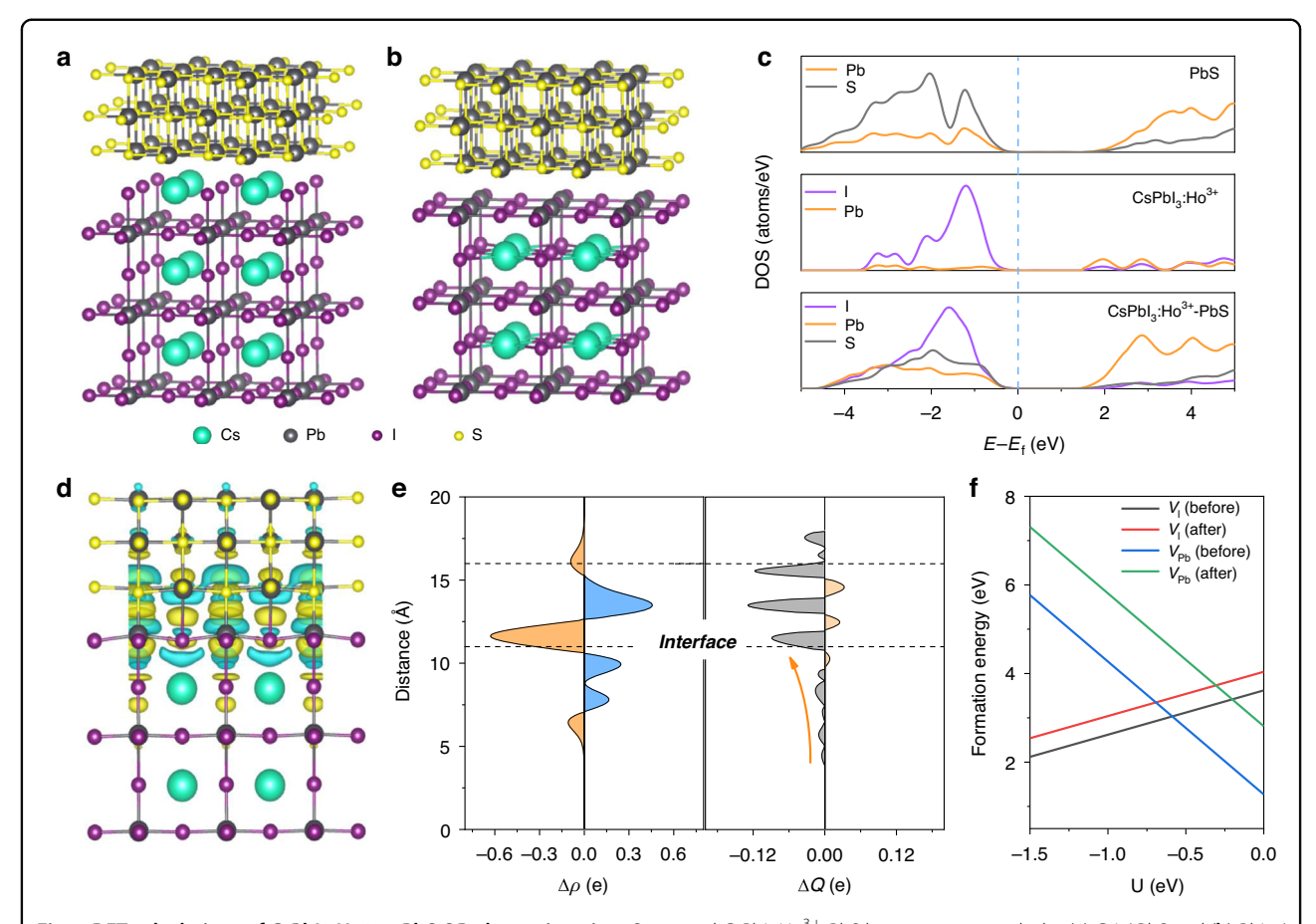


Fig. 4 DFT calculations of CsPbl3:Ho3+- PbS QDs heterojunction. Optimized CsPbl3:Ho³⁺-PbS heterojunction with the (**a**) CsI / PbS and (**b**) Pbl2 / PbS interfaces from side view. **c** Calculated DOS of the PbS, CsPbl3:Ho³⁺ and CsPbl3:Ho³⁺-PbS heterojunction. Charge density difference (**d**) x-y plane average charge difference and charge displacement curves along the z-direction of the Pbl2 / PbS interface (**e**). **f** The Pb vacancies (V_{Pb}) and I vacancies (V_{Pb}) defect formation energies for the CsPbl3:Ho³⁺ and CsPbl3:Ho³⁺ - PbS heterojunction with respect to the chemical potential of the I atom

To further investigate the charge recombination dynamic of CsPbI₃:Ho³⁺ PQDs after combining with the PbS QDs, the I-V curves of CsPbI₃:Ho³⁺ PQDs and CsPbI₃:Ho³⁺—PbS QDs heterojunction were measured (Fig. 3f). It can be seen that CsPbI₃:Ho³⁺ - PbS QDs heterojunction obtains higher σ (5.11×10⁻⁶ S cm⁻¹), compared with the CsPbI₃: Ho^{3+} PQDs device (3.54 × 10^{-6} S cm⁻¹). The ultraviolet photoelectron spectroscopy (UPS) was employed to determine the energy levels of the CsPbI₃:Ho³⁺ PQDs and PbS QDs (Fig. 3g, h). The valence band maximum (VBM) and the conduction band minimum (CBM) of CsPbI₃:Ho³⁺ PQDs and PbS QDs are deduced to be -5.65 eV and -5.31 eV, and -3.83 eV and -4.43 eV, respectively. As illustrated in Fig. 3i, the band alignment between CsPbI₃:Ho³⁺ PQDs and PbS QDs enables them to form a heterojunction. Under visible light illumination, the generated electrons in CsPbI₃:Ho³⁺ PQDs tends to enter electron transport layer (ETL, SnO₂). While the holes move to PbS QDs, subsequently transfer to hole transport layer (HTL, MoO₃). Meanwhile, the PbS QDs captures the NIR light to produce electrons and holes, the electrons transfer to ETL by CsPbI₃:Ho³⁺ PQDs, and the holes directly enter into HTL. Thus, the PDs combining CsPbI₃:Ho³⁺ PQDs with PbS QDs brings about the broadband response from visible to NIR-II.

The structural and photophysical interaction between of CsPbI₃:Ho³⁺ PODs and PbS ODs were calculated through density functional theory (DFT) (Supplementary Note 5). Figure 4a, b shows the optimized CsPbI₃:Ho³⁺—PbS QDs heterojunction with the PbI₂ / PbS and CsI / PbS interfaces. The adhesive energies of PbI2 / PbS interface (-3.22 eV) is smaller than that of the CsI / PbS interface (-2.07 eV), indicating that the PbI₂ / PbS is more stable interface structure⁵². The strong electron interface coupling between PbS and CsPbI₃:Ho³⁺ is revealed by the density of states (DOS) functional (Fig. 4c), where the significant overlap between the Pb 6p and I 5p states in CsPbI₃:Ho³⁺ PQDs with the S 2p orbital in PbS QDs. Furthermore, the bandgap of CsPbI₃:Ho³⁺—PbS QDs heterojunction shows a slight smaller than that of the CsPbI₃:Ho³⁺ PQDs, benefiting for the effectively transition of electrons from VBM to CBM. In order to understand the charge distribution of the CsPbI₃:Ho³⁺— PbS QDs heterojunction interface, the charge density difference $\Delta \rho$ is obtained by⁵³:

$$\Delta \rho = \rho_{hete} - \rho_{PbS} - \rho_{PODs} \tag{3}$$

where ρ_{hete} is the charge density of the fully relaxed CsPbI₃:Ho³⁺—PbS QDs heterojunction, ρ_{PbS} and ρ_{PQDs} are the isolated PbS QDs and CsPbI₃:Ho³⁺ PQDs slab. As shown in Fig. 4d, the charge depletions underneath Pb / I atoms for PbI₂ / PbS interface, which is favorable for efficient charge migration from CsPbI₃:Ho³⁺ PQDs to PbS QDs. Meanwhile, the x-y plane average charge difference Δq is calculated by⁵³:

$$\Delta q = \int_{-\infty}^{\infty} dy \int_{-\infty}^{\infty} \Delta \rho \, d\chi \tag{4}$$

In general, the charge accumulation and depletion can be obtained based on the positive and negative Δq , respectively⁵⁴. Fig. 4e displays the Δq of PbI₂ / PbS interface, where a dipole can be produced between the CsPbI₃:Ho³⁺ PQDs surface and PbS QDs because of the charge accumulation and depletion, facilitating the charge separation and transport. Moreover, the charge displacement (CD) functional (ΔQ) can be achieved through integrating the x-y plane average charge difference Δq along the z direction⁵²:

$$\Delta Q = \int_{-\infty}^{z} \Delta q \, dz \tag{5}$$

where the positive ΔQ values indicates the charge transfer from the right to the left across the perpendicular plane through this direction and vice versa. The CD plot of PbI₂ / PbS interface along z direction present that the whole negative for CsPbI₃:Ho³⁺ PQDs side, which means that the charge transport from CsPbI₃:Ho³⁺ PQDs to PbS QDs. As shown in Fig. 4f, we calculated the defect formation energies of Pb²⁺ vacancies (V_{Pb}) and I vacancies (V_{I}) in CsPbI₃:Ho³⁺ PQDs and CsPbI₃:Ho³⁺—PbS QDs heterojunction, where the V_{Pb} and V_{I} exhibit higher defect formation energies after PbS QDs coupling, benefiting for the responsivity of PDs²³.

To fabricate QC–LC, the cubic and uniform Cr^{3+} / Ce^{3+} / Yb^{3+} / Er^{3+} doped CsPbCl₃ PQDs with the average diameter of ~8.4 nm were prepared through the hot-injection method (Fig. S22)⁵⁵. The Cr^{3+} and Ce^{3+} were selected to improve emission intensity and boost DUV absorption of CsPbCl₃ PQDs. The emission of Yb³⁺ and Er^{3+} ions locate within the absorption of CsPbI₃:Ho³⁺—PbS QDs heterojunction, and has high efficient quantum cutting behavior in CsPbCl₃ PQDs. All the elements (Cs, Pb, Cl, Cr, Ce, Yb, and Er) exist in Cr^{3+} / Ce^{3+} / Yb^{3+} / Er^{3+} doped CsPbCl₃ PQDs (Fig. S23). Figure 5a displays the UV–Visible absorption spectra of undoped, Cr^{3+} doped CsPbCl₃ PQDs, Cr^{3+} / Yb^{3+} / Er^{3+}

doped CsPbCl₃ PQDs, and Cr³⁺ / Ce³⁺ / Yb³⁺ / Er³⁺ doped CsPbCl₃ PQDs. It can be seen that the absorption peak of CsPbCl₃ PODs locates at 405 nm, and blue shifts to 391 nm after Cr³⁺ / Ce³⁺ / Yb³⁺ / Er³⁺ doping, ascribed to the lattice contraction of PQDs by substituting Pb²⁺ with the smaller size doping ions 47,56 . Moreover, the absorption spectra of Cr $^{3+}$ / Ce $^{3+}$ / Yb $^{3+}$ / Er $^{3+}$ doped CsPbCl $_3$ PQDs present a significant enhancement within 200 nm-280 nm after Ce³⁺ doping, attributed to absorption contribution of 4f - 5d for Ce^{3+42} . Fig. 5b shows the emission spectra of PQDs, CsPbCl₃:Cr³⁺ CsPbCl₃ CsPbCl₃:Cr³⁺, Yb³⁺, Er³⁺ PQDs, and CsPbCl₃:Cr³⁺, Ce³⁺, Yb³⁺, Er³⁺ PQDs. It is found that an obvious exciton emission band centering at 410 nm for CsPbCl₃ PQDs was observed under 365 nm excitation, which significant improvement after Cr³⁺ doping. Except for exciton emission, two additional emission peaks in CsPbCl₃:Cr³⁺, Yb³⁺, Er³⁺ and CsPbCl₃:Cr³⁺, Ce³⁺, Yb³⁺, Er³⁺ PQDs were identified, appearing at 980 nm and 1540 nm, assigned to $Yb^{3+} (^2F_{5/2} - ^2F_{7/2})$ and $Er^{3+} (^4I_{13/2} - ^4I_{15/2})$. Similarly to the previous reported, they originate from the quantum cutting energy transfer from CsPbCl₃ PQDs to Yb³⁺, and further Yb³⁺ to Er^{3+57,58}. Furthermore, the introduction of Ce³⁺ regards as an intermediate bridge to match the energy between CsPbCl₃ PODs and NIR quantum cutting emission of Yb³⁺⁵⁹. Meanwhile, the PLQYs is estimated by²³:

$$PLQYs = \frac{N_{em}}{N_{abs}} = \frac{\int I_{sample}(\lambda) - I_{ref}(\lambda)d\lambda}{\int E_{ref}(\lambda) - E_{sample}(\lambda)d\lambda}$$
(6)

where N_{em} and N_{abs} are the number of emission and absorption photons of PQDs. I_{sample} and E_{sample} present the spectral intensity of the emitted light and excitation light of samples, and I_{ref} and E_{ref} are the spectral intensity of the emitted light and excitation light for a reference cuvette containing toluene. It should be highlighted that the PLQYs of CsPbCl₃:Cr³⁺, Ce³⁺, Yb³⁺, Er³⁺ PQDs reaches to 179% (Fig. 5c). The higher PLQYs are concluded in the following three aspects: (1) reduced k_{nr} of CsPbCl₃ PQDs after Cr³⁺ doping, (2) enhanced energy transfer from CsPbCl₃ PQDs to Yb³⁺ and improved DUV absorption after Ce³⁺, (3) NIR quantum cutting emission ($^2F_{5/2}$ - $^2F_{7/2}$) after Yb³⁺ doping. The energy transfer process for Cr³⁺, Ce³⁺, Yb³⁺, Er³⁺ doped CsPbCl₃ PQDs was represented in Fig. 5d.

Then, the CsPbCl₃:Cr³⁺, Ce³⁺, Yb³⁺, Er³⁺ PQDs were incorporated into a PMMA polymer matrix to form QC–LC. The performance of the QC–LC was achieved using an integrating sphere. As seen in Fig. 5e and S24, the QC–LC presents the similar emission spectra with CsPbCl₃:Cr³⁺, Ce³⁺, Yb³⁺, Er³⁺ PQDs and high transparency. Considering directly integrating one of edge of QC–LC with the PDs, the emission intensity of the edge, face, and total of LC were recorded (Fig. 5e). The emission intensity of the edge is higher than that of face, attributed to the waveguide effect of

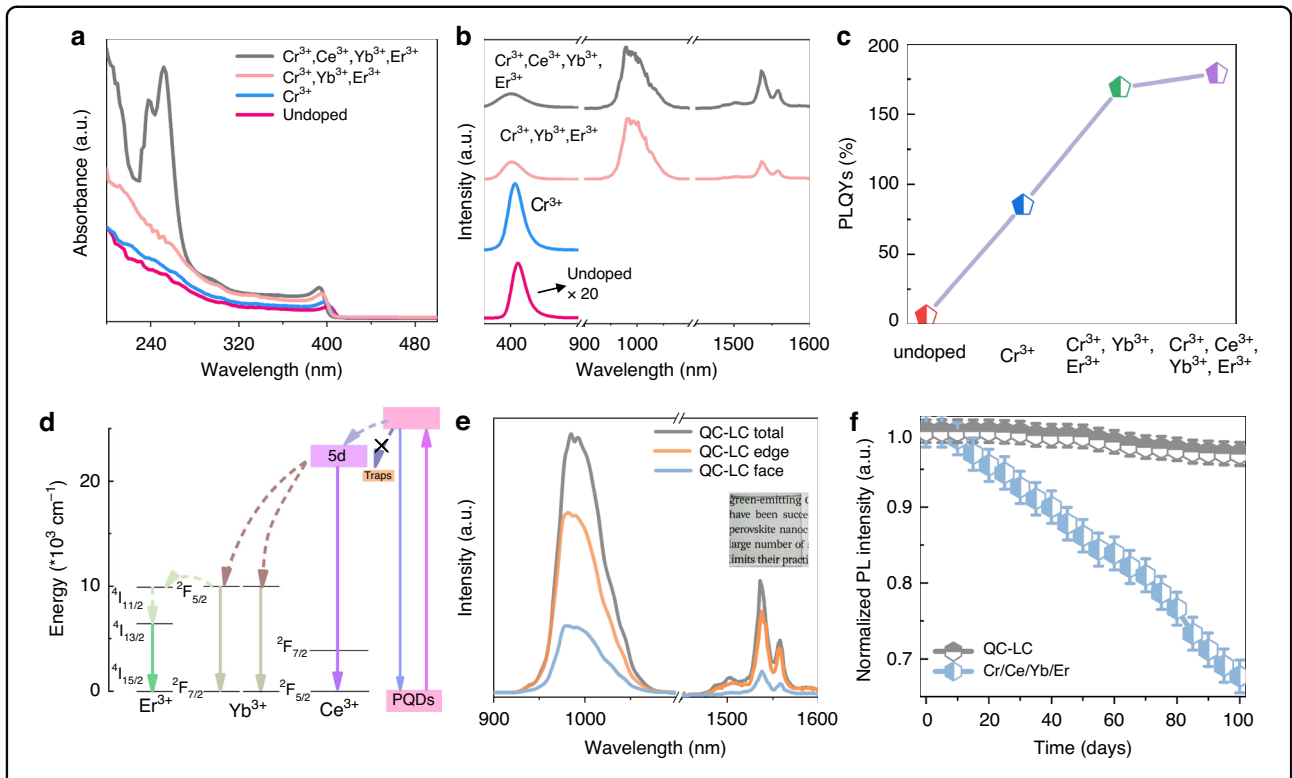


Fig. 5 Optical characteristics of QC-LC. Absorption spectra (**a**), emission spectra (**b**), and PLQYs (**c**) of undoped, Cr^{3+} , Cr^{3+} / Yb^{3+} / Er^{3+} , and Cr^{3+} / Ce^{3+} / Yb^{3+} / Er^{3+} doped $CsPbCl_3$ PQDs. **d** Energy level diagram of Cr^{3+} / Ce^{3+} / Yb^{3+} / Er^{3+} doped $CsPbCl_3$ PQDs. **e** The emission spectra of QC-LC using an integrating sphere method. To accuracy obtained the face emission spectra of QC-LC, the black tapes with high light absorption was used to the edges of QC-LC. The inset is the picture of QC-LC. **f** Normalized PL intensity of QC-LC and Cr^{3+} / Ce^{3+} / Yb^{3+} / Er^{3+} doped $CsPbCl_3$ PQDs films as a function of storage time

QC–LC. The edge and face emission intensity ratio of the QC-LC was 73.61%, which is nearly to the ideal light trapping efficiency of 75%^{13,60}. Moreover, the stability of CsPbCl₃:Cr³⁺, Ce³⁺, Yb³⁺, Er³⁺ PQDs were also remarkably enhanced by incorporating them into LC, in which their PL intensity remains 97.5% after 100 days storage (Fig. 5f). Based on the high luminescence performance and stability and transparency, the QC–LC can be severed as a converter to improve the DUV–UV responsivity for broadband PDs.

Figures 6a and S25 shows the photocurrent-time (I_p –t) response curves of FTO / SnO $_2$ / CsPbI $_3$ PQDs / MoO $_3$ / Au (PD1), FTO / SnO $_2$ / CsPbI $_3$:Ho $^{3+}$ PQDs / MoO $_3$ / Au (PD2), FTO / SnO $_2$ / CsPbI $_3$:Ho $^{3+}$ -PbS QDs heterojunction / MoO $_3$ / Au (PD3), and QC-LC / FTO / SnO $_2$ / CsPbI $_3$:Ho $^{3+}$ -PbS QDs heterojunction / MoO $_3$ / Au (PD4) in dark and 260 nm, 460 nm, and 1550 nm illumination at a bias of 0.5 V, respectively. It can be seen that the I $_p$ reach to 3.09 μ A of PD4, whereas only 0.84 μ A for PD1 under 460 nm illumination. Compared with the PD1, the I $_p$ of PD4 increase 3.68 folds for 460 nm, due to the reduce density of defects and boost carriers mobility after Ho $^{3+}$ doping, and passivized surface vacancy by PbS QDs. Besides, the dark current (I $_d$) of PD1–PD4 were recorded in Fig. S26. The value of I $_d$ was about 2.44 pA for PD1,

which decreases to 0.26 pA for PD4. Furthermore, the light to dark current ratio of PD4 was 1.19×10^7 , which further suggest the formation of uniform CsPbI₃:Ho³⁺— PbS QDs heterojunction film^{35,61}. Interestingly, the high I_p signals of DUV (0.91 μA of 260 nm) and NIR-II (0.64 µA of 1550 nm) were observed for PD4. The enhancement is mainly due to the strong absorption in the DUV region and extremely efficient NIR quantum cutting emission of QC-LC, and high performance NIR-II broadband absorption of PbS QDs. Figure 6b, c and S27-S28 shows the responsivity (R), detectivity (D*), and external quantum efficiency (EQE) of PD1-PD4 (Supplementary Note 6). Compared to the PD1 with lower R (119.04 mA $W^{\text{-}1})$ and D^{\ast} (5.43 $\times\,10^{11}$ Jones) and EQE (16.9%), the maximum R and D* and EQE of the PD4 were calculated to be 596.62 mA W⁻¹ and 1.05×10^{13} Jones and 84.6% under 460 nm illumination. Furthermore, these values of PD4 were largely enhanced in the DUV-UV and NIR-II region, realizing a broadband spectral response ranging from 200 nm to 1700 nm, where the R and D* and EQE of PD4 were 180.6 mA W-1 and 164.5 mA W^{-1} , $3.19 \times 10^{12} \text{ Jones and } 2.23 \times 10^{12} \text{ Jones}$, and 45.3% and 7.2% under 260 nm and 1550 nm, respectively. The statistical analysis on 25 devices for PD4 under

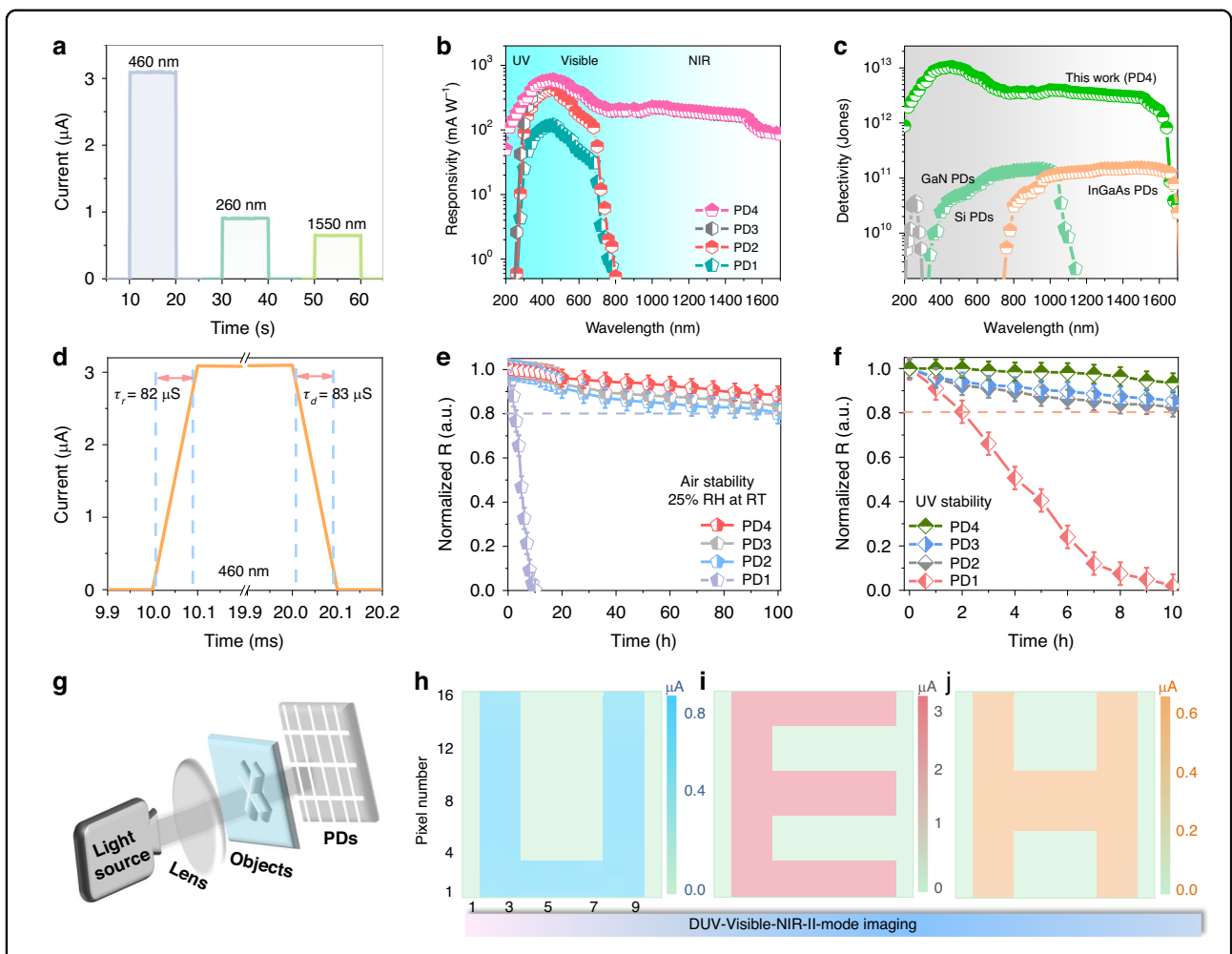


Fig. 6 Performances of PDs. a I_p –t curves of PD4 under the 260 nm, 460 nm, and 1550 nm illumination, respectively. **b** Responsivity of PD1–PD4. **c** Detectivity of this work (PD4), GaN PDs, Si PDs and InGaAs PDs, respectively. **d** Response time of the PD4 under 460 nm illumination. **e, f** The evolution of responsivity under 25% RH at room temperature and UV radiation. **g** Schematic diagram of imaging arrays. DUV–Visible-NIR-II mode imaging output for "U, E, H" mask under 260 nm (**h**), 460 nm (**i**) and 1550 nm (**j**), respectively

260 nm, 460 nm, and 1550 nm illumination, respectively, showing the excellent repeatability of this broadband PDs (Fig. S29). Importantly, the D* of PD4 improves two orders that of commercial GaN PDs and Si PDs and InGaAs PDs under the same detection condition. Meanwhile, the noise current (I_n) of PD4 (2.34 \times 10⁻¹⁴ A Hz^{-1/2}) was lower than that of PD1 (8.33 \times 10⁻¹⁴ A Hz^{-1/2}) at 1 Hz in Fig. S30. According to the noise-equivalent power (NEP) equation, the D* can also be calculation by ref. 6 :

$$D* = \frac{\sqrt{SB}}{NEP} (cmHz^{-\frac{1}{2}}W^{-1}or Jones)$$
 (7)

$$NEP = \frac{I_n}{R} \tag{8}$$

where S and B are the active layer area and the electrical bandwidth. The D^* of PD4 was obtained to be 7.71×10^{11}

Jones of $260 \, \text{nm}$, 2.55×10^{12} Jones of $460 \, \text{nm}$, and 5.23×10^{11} Jones of $1550 \, \text{nm}$, respectively (Fig. S31). Compared with the PD1, the D* of PD2–PD4 shows the consistent increases trend for it calculated by the dark current, indicating a great potential for weak light detection.

The photon-response times of PDs are exhibited in Fig. 6d and S33–S34. The rise (τ_r) and decay times (τ_d) of the PD4 were measured to be ~82 µs and ~83 µs under 460 nm illumination, much faster than that of the PD1 (~202 µs and ~223 µs). The fast response time can be attributed to the restrained defects after Ho³⁺ doping, and the enhanced charge extraction and transport by integrating with PbS QDs. Figure S35 represent the relative response trend versus the frequency of 460 nm light. The -3dB bandwidth of PD4 was calculated as 4.04 KHz, indicating a rapid response to 460 nm light signal. According to the law: $f_{-3dB} = 0.35/\tau_r^{62}$ the response time of PD4 is estimated to be 86.6 µs,

Table 1 Recent works of broadband PDs

Materials	D* (Jones)	R _t (μs)	Wavelength (nm)	Ref.
PEDOT:PSS / PbS / CsPbCl ₃	5.78 × 10 ¹⁰	=	350–1100	33
CH ₃ NH ₃ Pbl ₃ / C8BTBT	2.17×10^{12}	7.1×10^4	365-808	67
GeTe / WS ₂	1.67×10^{11}	3×10^{4}	450-980	68
PbS-SCN / CH ₃ NH ₃ Pbl ₃	3.0×10^{11}	4.2×10^4	365–1550	37
$PdSe_2 / FA_{1-x}Cs_xPbl_3$	~ 10 ¹³	3.5/4	200–1550	35
CH ₃ NH ₃ Pbl ₃ / PbSe	1.2×10^{8}	3×10^{3}	300-1500	61
CsPbBr ₃ / PbS QDs	1.13×10^{10}	11.5	400-1130	69
GQD-PEDOT: PSS / Si	8×10^{11}	80/70	300-1100	70
FAPbl ₃	9.4×10^{11}	6.1×10^4	340–700	71
$Gd_3Fe_5O_{12}$ / Gr / $Gd_3Fe_5O_{12}$ / MoS_2	4.504×10^{12}	$2.9 \times 10^5 / 4.9 \times 10^5$	300-1500	72
CQDs-halide / CQDs-EDT	2.5×10^{12}	7.79/11.48	400-1400	73
2D Bi ₂ O ₂ Se / CsBi ₃ l ₁₀	1.22×10^{12}	4.1/6.2	365–1500	74
p-WSe ₂ / n-Ge	2.1×10^{10}	30	450-1550	75
Bi ₂ Te ₃ -SnSe-Bi ₂ Te ₃	6×10^{10}	=-	370-808	76
$FA_{0.5}MA_{0.45}Cs_{0.05}Pb_{0.5}Sn_{0.5}I_3$	2.21×10^{11}	0.043	300-1050	6
MoS_2 / CdTe	6.1×10^{10}	43.7/82.1	200-1700	77
FAMAPbl ₃	4.3×10^{12}	6.3×10^4	300-800	78
PEDOT: PSS / PbS / CsPbCl ₃	6.77×10^{12}	6.5×10^5	405-808	36
CH ₃ NH ₃ Pbl ₃	~10 ¹¹	4.1/3.6	300–750	79
Cr/Ce/Mn-LC / CsPbl ₃ :Er ³⁺ / BHJ	2.46×10^{12}	350/300	200-1000	23
QC-LC / FTO / SnO ₂ / CsPbl ₃ :Ho ³⁺ -PbS QDs / MoO ₃ / Au	1.05×10 ¹³	82/83	200-1700	This wor

similar to the response time measured in Fig. 6d. Furthermore, compared to the recent works of broadband PDs (Table 1 and Fig. S36), this broadband PDs shows the higher D* and faster response time from DUV to NIR-II regions. As shown in Fig. S37, the R as a function of light power density (P) can be fitted by the formula: $R \propto P^{\alpha 63}$ where α were achieved to be 0.67, 0.56, and 0.66 for PD4 under 260 nm, 460 nm, and 1550 nm, respectively. The α value of the PD4 is not closer to ideal result ($\alpha = 1$), suggesting that defects still exist in the heterojunction interface^{64–66}. Figure 6e, f displays the normalized R variation curves of PD1-PD4 at humidity of 25% and under UV irradiation at room temperature. The R of the PD1 declines to 0% after 100 h storage and 10 h UV irradiation, while the R of the PD4 remained 89% and 99.3% for the original Rvalue after 100 h storage and 10 h UV irradiation. The enhanced air- and UV- stability of PDs would be attributed to the Ho³⁺ doping, PbS QDs hybridization, and the buffer layer of QC-LC in the devices.

Based on the outstanding DUV-Visible-NIR-II detection performance, the imaging application of this

broadband PD was further explored. As presented in Fig. 6g, the imaging schematic is composed by different light source (DUV of 260 nm, Visible of 460 nm, and NIR-II of 1550 nm), lens, object letters ("U", "E", and "H"), broadband PDs and signal collector. We fabricated a 10×16 pixel detector array as the each photograph shown in Fig. 6h-j. The thickness of the detectors is 1 mm and the electrode area of each pixel is $1 \times 1 \text{ mm}^2$. It can be seen that the letters were clearly achieved with high light to dark current ratios under different illuminations, highlighting that the excellent performance of broadband detection and imaging capability for the QC-LC / FTO / SnO₂ / CsPbI₃:Ho³⁺-PbS QDs heterojunction / MoO₃ / Au PDs. Moreover, these results strongly indicate that the remarkable adaptability of the PDs and great promising for broadband imaging without low temperature working conditions.

Discussion

In this work, an excellent performance DUV-Visible-NIR-II broadband PD was successfully fabricated based

on QC-LC and CsPbI₃:Ho³⁺—PbS QDs heterojunction, exhibiting the high detectivity of 3.19×10^{12} Jones at 260 nm, 1.05×10^{13} Jones at 460 nm, and 2.23×10^{12} Jones at 1550 nm, respectively. The optimized CsPbI₃:Ho³⁺ PQDs demonstrated low trap density and high charge mobility compared with the undoped CsPbI₃ PQDs, enabling superb responsivity and detectivity of visible region. Then, the hybridization of CsPbI₃: Ho³⁺—PbS QDs heterojunction successfully expand the response of broadband PDs to the NIR-II region, due to the narrow bandgap and large absorption coefficient of PbS QDs. Meanwhile, high efficiency NIR quantum cutting emission (PQLYs ~ 179%) and strong DUV-UV absorption of Cr³⁺, Ce³⁺, Yb³⁺, Er³⁺ doped CsPbCl₃ PQDs were embedded to form QC-LC, which can be integrated with the FTO side to improve the responsivity of PDs for DUV-UV light. Our work shows a promising path for fabricated the high performancebroadband PDs and imaging capability.

Materials and methods

Materials

 Cs_2CO_3 (99.9%), 1-octadecene (ODE, 90%), oleic acid (OA, 85%), oleylamine (OAm, 70%), PbO (99.99%), PbI₂ (99.99%), HoI₃ (99.99%), PbCl₂ (99.9%), CrCl₃ (99.99%), CeCl₃ (99.99%), YbCl₃ (99.99%), ErCl₃ (99.99%), bis(trimethylsilyl) sulfide, toluene, cyclohexane and ethyl acetate (99%) were purchased from Mackline and were used without further purification.

Synthesis of CsPbl₃ PQDs

0.8 g Cs2CO3 was added into a mixture of 30 mL of ODE and OA (2.5 mL) and then heated to 150 °C until the white powder was completely dissolved. The mixture was then kept at 120 °C to obtained the Cs-oleate. Then, PbI2 (0.3 mmol), OAm (1.5 mL), OA (1.5 mL), and ODE (10 mL) were added to a 50-mL 3-neck round-bottomed flask and were evacuated with N2, by heating the solution to 120 °C for 1 h. The temperature of the solution was then increased to 180 °C for 10 min. Finally, the Cs-oleate (1 mL) was swiftly injected into the solution. After 10 s, the solution was cooled in an ice bath. The CsPbI₃ PQDs were precipitated and then centrifuged, followed by dissolution in toluene.

Synthesis of CsPbl₃:Ho³⁺ PQDs

 HoI_3 (x mmol), PbI_2 (0.3 mmol), OAm (1.5 mL), OA (1.5 mL), and ODE (10 mL) were adequately dissolved at 120 °Cfor 1 h under purging N_2 gas. The following steps were the same with synthesis of CsPbI₃ PQDs.

Synthesis of Cr³⁺,Ce³⁺,Yb³⁺,Er³⁺ doped CsPbCl₃ PQDs

For the CsPbCl3: Cr³⁺, Ce³⁺, Yb³⁺, Er³⁺ PQDs, PbCl2 (0.5 mmol), CrCl3 (0.3 mmol), CeCl₃(0.2 mmol), YbCl3

(0.3 mmol), ErCl3 (0.2 mmol) were loaded into round-bottom flask with ODE (10 mL), OAm (1.5 mL) and OA (1.5 mL). The following steps were the same with the synthesis of the Ho^{3+} doped CsPbI₃ PQDs.

Fabrication of QC-LC

 $0.8\,\mathrm{g}$ PMMA (MW ~ 350000) was dispersed in 5 mL toluene by sonication, where toluene solution (3 mL) of CsPbCl3: Cr³+, Ce³+, Yb³+, Er³+ PQDs were added. The mixture was sealed and stirred overnight to obtain homogenous slurry. The slurry was centrifuged at 2000 rpm and the supernatants were used for LC fabrication. The above supernatants were spin-coating onto borosilicate glass substrates.

Syntheses of PbS QDs

Firstly, PbO (0.36 g), OA (1 mL), and ODE (15 mL) were stirred and heated to 145 °C under nitrogen atmosphere. Then, ODE (4.0 mL) containing bis (trimethylsilyl) sulfide (168 μL) was quickly injected into the reaction flask, and meanwhile the heater was switched off. The hot solution was naturally cooled down, and the formed oil-soluble PbS QDs were precipitated. The purification was carried by isopropyl alcohol and acetone. Finally, the PbS CQDs were dispersed in toluene to produce a 50 mg mL $^{-1}$ solution.

Preparation of the CsPbI₃:Ho³⁺-PbS QDs heterojunction composite

In a typical procedure, a $200\,\mu L$ CsPbI $_3$:Ho $^{3+}$ solution (10 mg mL $^{-1}$, toluene) was mixed with 2 mL of PbS solution (1 mg mL $^{-1}$, toluene), and the total volume remained at 5 mL. Under dark conditions, the suspension was ultrasonicated for 10 min and stirred for 0.5 h. Finally, the CsPbI $_3$:Ho $^{3+}$ —PbS CQDs heterojunction composites were collected by centrifuging at 8000 rpm for 5 min.

Device fabrication

FTO coated glass substrates were etched by zinc powder and HCl to define the electrode patterns and washed in deionized water, acetone, and ethanol for 20 min, respectively. The ultraviolet-ozone was used to remove the organic residues of FTO surface. To fabricate the compact SnO₂ layer, the SnO₂ colloid solution by water to the concentration of 2.14 wt% and was spin-coated on FTO substrates at 5000 rpm for 30 s and then annealed at 150 °C for 30 min. The CsPbI₃:Ho³⁺—PbS CQDs heterojunction film was fabricated on the SnO₂ layer by spincoating at 2000 rpm for 40 s. For broadband PDs, MoO3 and Au was evaporated on CsPbI₃:Ho³⁺—PbS CQD film layer. Then, the edge surface of QC-LC with the edge size of 1×0.4 mm² was attached and fixed to the ITO layer of PD with area of $1 \times 1 \text{ mm}^2$. When UV light radiation on the face of QC-LC, then the emitted 400-1700 nm light is coupled out of the edge surface into the FTO of PDs. The visible and NIR lights directly pass through the FTO and reach the PD. Because the QC–LC only occupies a part of surface of the FTO layer and has high transparency for photons with the longer wavelength (>400nm), which would not affect the light collection of PDs.

Characterization

UV/vis-NIR absorption spectra were measured with a Shimadzu UV-3600PCscanning spectrophotometer in the range from 200 to 2500 nm. Patterns were recorded in thin film mode on a Bruker AXS D8 diffractmeter by Cu Karadiation ($\lambda = 1.54178 \,\text{Å}$). Atomic Force Microscope was texted using a DI Innova AFM (Bruker) in light tapping mode. The morphology of the products was recorded with a Hitachi H-8100IV transmission electron microscope (TEM) under an acceleration voltage of 200 kV. A Visible-NIR photomultiplier combined with a double-grating monochromator were used for spectral collection. The X-ray photoelectron spectroscopy (XPS) was carried out in a Kratos Axis Ultra DLD spectrometer equipped with a monochromatic Al Ka X-ray source (hv = 1486.6 eV) operated at 150 W with a multichannel plate, and a delay line detector under 1.0×10^{-9} Torr vacuum. Nanosecond fluorescence lifetime experiments were performed by the time correlated single-photon counting system. The Mott-Schottky curves via capacitance-voltage measurements of CsPbI₃:Ho³⁺ PQDs were obtained by a Princeton electrochemical workstation. The Xe lamp with the spectral range from 200 nm to 2500 nm equipped with a monochromator was used to generate the monochromatic light to conduct the spectral response measurements. Actually, the intensity of Xe lamp is weak in the region of 200 nm-300 nm, thus we must correct it before the measurement.

Acknowledgements

This work was supported by the Artificial Intelligence Innovation and Development Foundation of Liaoning Province (2023JH26/10300023), the National Natural Science Foundation of China (12404450, U21A2074, 11974143, 11974069, 62305045, 12104084 and 62222502), the Liaoning Bai Qian Wan Talents Program (2021921012), the Young Top Talents of Liaoning Province Xingliao Talent Plan (XLYC2203170), the Science and Technique Foundation of Dalian (2022JJ11CG003), the Science and Technique Foundation of Liaoning Province (2023JH1/10400057, 2023JH1/10400080, 2023JH2/101700309), the Outstanding Young Scientific and Technological Talents of Dalian (2021RJ07), the Basic Scientific Research Project of Education Department of Liaoning Province (LJKQZ20222455), the Dalian Science and Technology Talents Innovation Support Program Project (2022RQ020), State Key Laboratory of Advanced Optical Communication Systems and Networks (2023GZKF06), and the Fundamental Research Funds for the Central Universities (04442024071).

Author contributions

N.D., W.X., and H.L. conceived the idea and initiated the project. Y.J., Z.W. and Y.J. designed the experiments and supervised the project. J.W. and L.S. synthesized the quantum dots and fabricated the devices. G.Z. and Y.J. tested the PDs. N.D. processed the data. H.L. analyzed the experimental results. N.D., W.X., and B.D. wrote the manuscript.

Conflict of interest

The authors declare no competing interest.

Supplementary information The online version contains supplementary material available at https://doi.org/10.1038/s41377-024-01604-0.

Received: 19 April 2024 Revised: 30 July 2024 Accepted: 23 August 2024 Published online: 15 October 2024

References

- Guo, Z. N. et al. In-situ neutron-transmutation for substitutional doping in 2D layered indium selenide based phototransistor. *eLight* 2, 9 (2022).
- Dong, H. Metal Halide Perovskite for next-generation optoelectronics: progresses and prospects. eLight 3, 3 (2023).
- Wang, P. S. et al. Van der Waals two-color infrared photodetector. Light Sci. Appl. 11, 6 (2022).
- Ji, Y. N. et al. Semiconductor plasmon enhanced monolayer upconversion nanoparticles for high performance narrowband near-infrared photodetection. Nano Energy 61, 211–220 (2019).
- Chen, X. X. et al. Ultrasensitive broadband position-sensitive detector based on graphitic carbon nitride. Nano Res. 16, 1277–1285 (2023).
- Ma, N. N. et al. Stable and sensitive tin-lead perovskite photodetectors enabled by azobenzene derivative for near-infrared acousto-optic conversion communications. *Nano Energy* 86, 106113 (2021).
- Hu, W. et al. Germanium/perovskite heterostructure for high-performance and broadband photodetector from visible to infrared telecommunication band. Light Sci. Appl. 8, 106 (2019).
- 8. Zhang, M. J. et al. Perovskite quantum dots embedded composite films enhancing UV response of silicon photodetectors for broadband and solar-blind light detection. *Adv. Opt. Mater.* **6**, 1800077 (2018).
- Cao, G. Q. et al. Multicolor broadband and fast photodetector based on InGaAs-insulator-graphene hybrid heterostructure. Adv. Electron. Mater. 6, 1901007 (2020).
- Khan, J. et al. Tuning the surface-passivating ligand anchoring position enables phase robustness in CsPbl₃ perovskite quantum dot solar cells. ACS Energy Lett. 5, 3322–3329 (2020).
- Wang, Y. et al. Surface ligand management aided by a secondary amine enables increased synthesis yield of CsPbl₃ perovskite quantum dots and high photovoltaic performance. Adv. Mater. 32, 2000449 (2020).
- Ding, N. et al. Upconversion ladder enabled super-sensitive narrowband nearinfrared photodetectors based on rare earth doped florine perovskite nanocrystals. Nano Energy 76, 105103 (2020).
- Luo, X. et al. Quantum-cutting luminescent solar concentrators using ytterbium-doped perovskite nanocrystals. Nano Lett. 19, 338–341 (2019).
- Yang, G. et al. Efficient quantum cutting of lanthanum and ytterbium ions codoped perovskite quantum dots towards improving the ultraviolet response of silicon-based photodetectors. J. Alloy. Comp. 921, 166097 (2022).
- Xu, W. et al. Atomic-scale imaging of ytterbium ions in lead halide perovskites. Sci. Adv. 9, eadi7931 (2023).
- Liu, K. K. et al. Water-induced MAPbBr₃@PbBr(OH) with enhanced luminescence and stability. Light Sci. Appl. 9, 44 (2020).
- Bi, C. H. et al. Improved stability and photodetector performance of CsPbl₃ perovskite quantum dots by ligand exchange with aminoethanethiol. *Adv. Funct. Mater.* 29, 1902446 (2019).
- Zhao, C. et al. Polymer-assisted phase stable γ-CsPbl₃ perovskite film for self-powered and ultrafast photodiodes. Adv. Mater. Interf. 9, 2102212 (2022).
- Kim, H. et al. Bias-modulated multicolor discrimination enabled by an organicinorganic hybrid perovskite photodetector with a p-i-n-i-p configuration. *Laser Photon. Rev.* 14, 2000305 (2020).
- Liu, K. L. et al. Highly efficient and stable red perovskite quantum dots through encapsulation and sensitization of porous CaF₂: Ce, Tb nanoarchitectures. Nanoscale 14, 4263–4270 (2022).
- Shen, X. Y. et al. Zn-alloyed CsPbl₃ nanocrystals for highly efficient perovskite light-emitting devices. Nano Lett. 19, 1552–1559 (2019).
- Shao, L. et al. Near-infrared-pumped photon upconversion in CsPbl₃ and CaF₂: Yb³⁺/Ho³⁺ nanocomposites for bio-imaging application. *Mater. Today Phys.* 21, 100495 (2021).

- Ding, N. et al. A novel approach for designing efficient broadband photodetectors expanding from deep ultraviolet to near infrared. *Light Sci. Appl.* 11, 91 (2022).
- Sulaman, M. et al. Hybrid bulk-heterojunction of colloidal quantum dots and mixed-halide perovskite nanocrystals for high-performance self-powered broadband photodetectors. Adv. Funct. Mater. 32, 2201527 (2022).
- Ding, N. et al. Europium-doped lead-free Cs₃Bi₂Br₉ perovskite quantum dots and ultrasensitive Cu²⁺ detection. ACS Sustain. Chem. Eng. 7, 8397–8404 (2019).
- Zhong, Y. et al. Circularly polarized luminescence of lanthanide complexes: from isolated individuals, discrete oligomers, to hierarchical assemblies. *Info-Mat* 5, e12392 (2023).
- Jin, S. L. et al. Compact ultrabroadband light-emitting diodes based on lanthanide-doped lead-free double perovskites. Light Sci. Appl. 11, 52 (2022).
- Zhang, G. D. et al. Er³⁺/Yb³⁺-based halide double perovskites with highly efficient and wide ranging antithermal quenching photoluminescence behavior for light-emitting diode applications. *Laser Photon. Rev.* 16, 2200078 (2022).
- Ding, N. et al. Highly-sensitive, stable, and fast-response lead-free Cs₂AgBiBr₆ double perovskite photodetectors enabled by synergistic engineering of doping Na⁺/Ce³⁺ and integrating Ag nanoparticles film. *Laser Photon. Rev.* 16, 2200301 (2022).
- Wang, L. et al. Exploration of nontoxic Cs₃CeBr₆ for violet light-emitting diodes. ACS Energy Lett. 6, 4245–4254 (2021).
- Chiba, T. et al. Neodymium chloride-doped perovskite nanocrystals for efficient blue light-emitting devices. ACS Appl. Mater. Interf. 12, 53891–53898 (2020)
- Zi, L. et al. X-ray quantum cutting scintillator based on CsPbCl_xBr_{3-x}: Yb³⁺ single crystals. Laser Photon. Rev. 17, 2200852 (2023).
- Zhao, X. H. et al. Vertically stacked PEDOT: PSS/PbS/CsPbCl₃ for flexible optoelectronic devices. J. Alloy Comp. 866, 158997 (2021).
- Li, K. et al. Vertically stacked Au/PbS/CsPbCl₃ phototransistors for plasmonenhanced high-performance broadband photodetection. ACS Appl. Electron. Mater. 2, 4080–4086 (2020).
- Zeng, L. H. et al. Multilayered PdSe₂/perovskite Schottky junction for fast, selfpowered, polarization-sensitive, broadband photodetectors, and image sensor application. Adv. Sci. 6, 1901134 (2019).
- Zhao, X. H. et al. Enhanced photodetection of perovskite nanoplatelet devices by vertically stacked PEDOT: PSS/PbS/CsPbCl₃ architecture. Mater. Lett. 290, 129467 (2021).
- Zhang, J. Y. et al. Toward broadband imaging: surface-engineered PbS quantum dot/perovskite composite integrated ultrasensitive photodetectors. ACS Appl. Mater. Interf. 11, 44430–44437 (2019).
- Liu, Q. B. et al. Epitaxial growth of CsPbBr₃-PbS vertical and lateral heterostructures for visible to infrared broadband photodetection. *Nano Res.* 14, 3879–3885 (2021).
- Kang, C. H. et al. High-speed colour-converting photodetector with allinorganic CsPbBr₃ perovskite nanocrystals for ultraviolet light communication. *Light Sci. Appl.* 8, 94 (2019).
- Wu, Y. J. et al. Toward broad spectral response inverted perovskite solar cells: insulating quantum-cutting perovskite nanophosphors and multifunctional ternary organic bulk-heterojunction. Adv. Energy Mater. 12, 2200005 (2022).
- Lyu, J. K. et al. Ni²⁺ and Pr³⁺ Co-doped CsPbCl₃ perovskite quantum dots with efficient infrared emission at 1300 nm. *Nanoscale* 13, 16598–16607 (2021).
- Li, D. Y. et al. Cerium-doped perovskite nanocrystals for extremely highperformance deep-ultraviolet photoelectric detection. Adv. Opt. Mater. 9, 2100423 (2021).
- Sun, R. et al. In situ preparation of two-dimensional ytterbium ions doped allinorganic perovskite nanosheets for high-performance visual dual-bands photodetectors. *Nano Energy* 93, 106815 (2022).
- Li, S. et al. Sodium doping-enhanced emission efficiency and stability of CsPbBr₃ nanocrystals for white light-emitting devices. *Chem. Materials* 31, 3917–3928 (2019).
- Sun, R. et al. Efficient single-component white light emitting diodes enabled by lanthanide ions doped lead halide perovskites via controlling Forster energy transfer and specific defect clearance. *Light Sci. Appl.* 11, 340 (2022).
- Hao, M. Y. et al. Dy³⁺ doped all-inorganic perovskite nanocrystals glass toward high-performance and high-stability silicon photodetectors. *Laser Photon. Rev.* 17, 2200748 (2023).
- Pan, G. C. et al. Doping lanthanide into perovskite nanocrystals: highly improved and expanded optical properties. Nano Lett. 17, 8005–8011 (2017).

- Ding, J. et al. Eu³⁺ doped CsPbCl₂Br₁ nanocrystals glass for enhanced the ultraviolet response of Si photodetectors. J. Lumin. 254, 119530 (2023).
- Protesescu, L. et al. Nanocrystals of cesium lead halide perovskites (CsPbX₃, X = Cl, Br, and I): novel optoelectronic materials showing bright emission with wide color gamut. Nano Lett. 15, 3692–3696 (2015).
- Wang, K. et al. Efficient perovskite solar cells by hybrid perovskites incorporated with heterovalent neodymium cations. Nano Energy 61, 352–360 (2019).
- Liu, J. et al. Flexible and broadband colloidal quantum dots photodiode array for pixel-level X-ray to near-infrared image fusion. *Nat. Commun.* 14, 5352 (2023).
- Cao, Y. H. et al. Asymmetric strain-introduced interface effect on the electronic and optical properties of the CsPbl₃/SnS van der Waals heterostructure. Adv. Mater. Interf. 6. 1901330 (2019).
- Liu, B. et al. Two-dimensional van der Waals heterostructures constructed via perovskite (C₄H₉NH₃)₂XBr₄ and black phosphorus. *J. Phys. Chem. Lett.* 9, 4822–4827 (2018).
- Volonakis, G. & Giustino, F. Ferroelectric graphene–perovskite interfaces. J. Phys. Chem. Lett. 6 2496–2502 (2015).
- Ding, N. et al. Extremely efficient quantum-cutting Cr³⁺, Ce³⁺, Yb³⁺ tridoped perovskite quantum dots for highly enhancing the ultraviolet response of silicon photodetectors with external quantum efficiency exceeding 70. Nano Energy 78, 105278 (2020).
- Zhao, J. et al. Efficient dual-mode emissions of high-concentration erbium ions doped lead-free halide double perovskite single crystals. J Alloy Comp. 895, 162601 (2022).
- Milstein, T. J., Kroupa, D. M. & Gamelin, D. R. Picosecond quantum cutting generates photoluminescence quantum yields over 100% in ytterbium-doped CsPbCl₃ nanocrystals. *Nano Letters* 18, 3792–3799 (2018).
- Zhu, Y. S. et al. Effective infrared emission of erbium ions doped inorganic lead halide perovskite quantum dots by sensitization of ytterbium ions. *J. Alloy Comp.* 835, 155390 (2020).
- Zhou, D. L. et al. Cerium and ytterbium codoped halide perovskite quantum dots: a novel and efficient downconverter for improving the performance of silicon solar cells. Adv. Mater. 29, 1704149 (2017).
- Wu, K. F., Li, H. B. & Klimov, V. I. Tandem luminescent solar concentrators based on engineered quantum dots. *Nature Photon.* 12, 105–110 (2018).
- Yu, Y. et al. Broadband phototransistor based on CH₃NH₃Pbl₃ perovskite and PbSe quantum dot heterojunction. J. Phys. Chem. Lett. 8, 445–451 (2017).
- He, M. et al. Sn-based self-powered ultrafast perovskite photodetectors with highly crystalline order for flexible imaging applications. *Adv. Funct. Mater.* 33, 2300282 (2023).
- Gong, M. G. et al. High-performance all-inorganic CsPbCl₃ perovskite nanocrystal photodetectors with superior stability. ACS Nano 13, 1772–1783 (2019).
- Dubey, A. et al. Aluminum plasmonics enriched ultraviolet GaN photodetector with ultrahigh responsivity, detectivity, and broad bandwidth. *Adv. Sci.* 7, 2002274 (2020).
- Wang, F. K. et al. 2D metal chalcogenides for IR photodetection. Small 15, 1901347 (2019).
- Kim, H. et al. Solution-processed phototransistors combining organic absorber and charge transporting oxide for visible to infrared light detection. ACS Appl. Mater. Interf. 11, 36880–36885 (2019).
- Xia, H. Y. et al. Flexible and air-stable perovskite network photodetectors based on CH₃NH₃Pbl₃/C8BTBT bulk heterojunction. *Appl. Phys. Lett.* **112**, 233301 (2018).
- Qu, J. Y. et al. Space-confined growth of ultrathin P-type GeTe nanosheets for broadband photodetectors. Small. 20, 2309391 (2024).
- Zhao, H. L. et al. Self-driven visible-near infrared photodetector with vertical CsPbBr₃/PbS quantum dots heterojunction structure. *Nanotechnology* 31, 035202 (2020).
- Tsai, M. L. et al. Omnidirectional harvesting of weak light using a graphene quantum dot-modified organic/silicon hybrid device. ACS Nano 11, 4564–4570 (2017).
- Wang, M. et al. Moisture-triggered self-healing flexible perovskite photodetectors with excellent mechanical stability. Adv. Mater. 33, 2100625 (2021)
- Zhang, Z. et al. High-performance broadband flexible photodetector based on Gd₃Fe₅O₁₂-assisted double van der Waals heterojunctions. *Microsyst. Nanoeng.* 9, 84 (2023).
- Liu, P. L. et al. Double-ended passivator enables dark-current-suppressed colloidal quantum dot photodiodes for CMOS-integrated infrared imagers. *InfoMat* 6, e12497 (2024).

- Dang, L. Y. et al. Efficient carrier transport in 2D Bi₂O₂Se/CsBi₃I₁₀ perovskite heterojunction enables highly-sensitive broadband photodetection. Small 20, 2306600 (2024).
- 75. Lee, C. H. et al. Design of p-WSe₂/n-Ge heterojunctions for high-speed broadband photodetectors. *Adv. Funct. Mater.* **32**, 2107992 (2022).
- Yao, J. D., Zheng, Z. Q. & Yang, G. W. All-layered 2D optoelectronics: a highperformance UV-vis-NIR broadband SnSe photodetector with Bi2Te3 topological insulator electrodes. Adv. Funct. Mater. 27, 1701823 (2017).
- Wang, Y. G. et al. A room-temperature near-infrared photodetector based on a MoS₂/CdTe p-n heterojunction with a broadband response up to 1700 nm. *J. Mater. Chem. C* 6, 4861–4865 (2018).
- 78. Wu, J. J. et al. Constructing high-performance solar cells and photodetectors with a doping-free polythiophene hole transport material. *Adv. Funct. Mater.* **34**, 2308584 (2024).
- He, J. et al. Improving photoelectric conversion with broadband perovskite metasurface. Nano Lett. 22, 6655–6663 (2022).